

## Supplementary Information

### Revealing high coercivity in Nd-Fe-B with gradient rare earth-rich phase sizes

Dongmin Zhang,<sup>a</sup> Minggang Zhu,<sup>\*ab</sup> Jingyan Zuo,<sup>a</sup> Qisong Sun,<sup>a</sup> Xiaolong Song,<sup>a</sup> Xian Wu,<sup>a</sup> Wei Li<sup>a</sup>

<sup>a</sup> Division of Functional Materials, Central Iron and Steel Research Institute, Beijing 100081, China

<sup>b</sup> School of Materials Science and Engineering, Northeastern University, Shenyang 110819, China

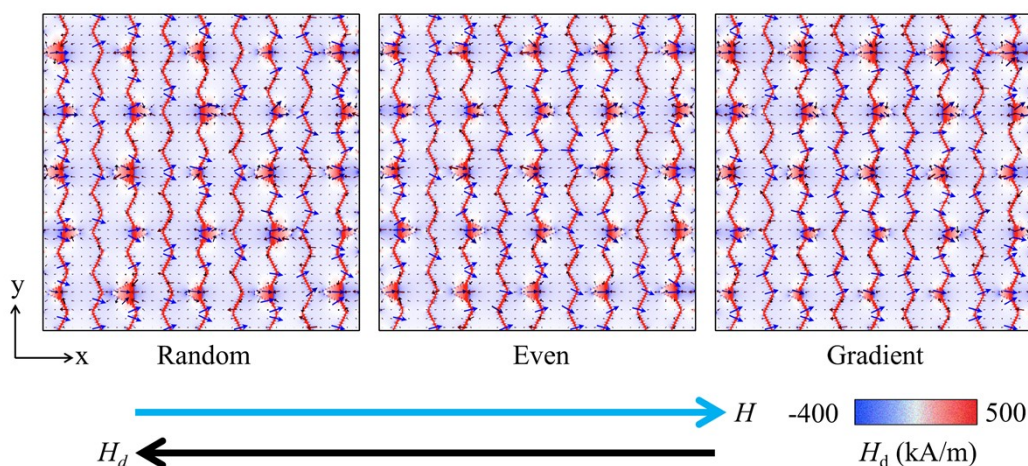


**Fig. S1** Simulation of the demagnetizing field for RERPs with different sizes and distributions in the saturated magnetization state. RERP sizes at random spatial distribution (left), even spatial distribution (middle) and gradient spatial distribution (right) show chaotic, uniform and gradient demagnetizing field distributions. The easy magnetization axis of the model and the direction of magnetic field application are both horizontally to the right.

As a vector field, the spatial distribution of the demagnetizing field  $H_d$  contains both direction and intensity information. The vector properties of  $H_d$  are synergistically characterized by two visualization schemes, the planar pixel filling and the arrow marking, which are defined as follows:

#### 1. Planar pixel filling

- Color hue: reflecting the direction information of the  $H_d$ .
- Color shade: reflecting the magnitude of the  $H_d$ .

## 2. Arrow marking

- Arrow pointing: visualization of the spatial direction of  $H_d$ .
- Arrow size: characterizes the magnitude of  $H_d$  by its length and thickness.

Arrow Color: Coupled with the color scale diagram rule to further enhance the visual recognition of direction and magnitude. A red-black-blue linear colormap is used, which strictly corresponds to the x-direction component of the  $H_d$ . Red→black→blue corresponds to a continuous variation of  $H_{d,x}$  from negative maxima (-x direction, opposite to the applied magnetic field direction)→0 (in the yz plane)→positive maxima (+x direction, along the applied magnetic field direction).

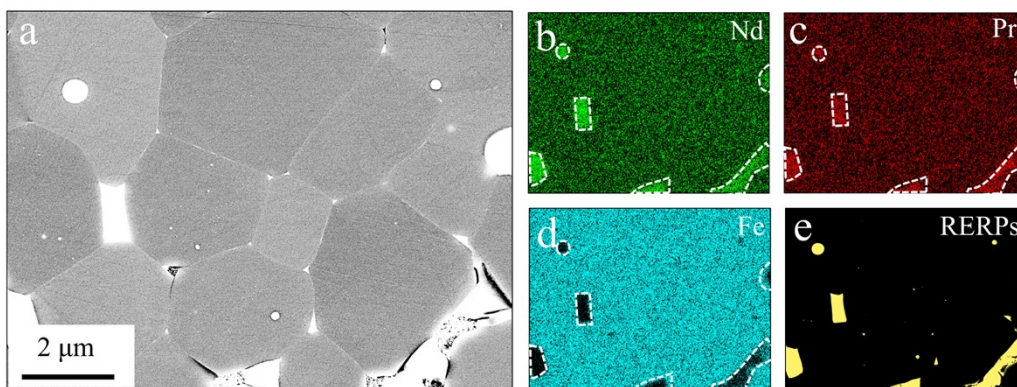


**Fig. S2** Microstructural characterization of RERPs within G-3 ( $l=32$  mm). (a) Typical BSE image, (b-d) EDS elemental maps for Nd, Pr and Fe. (e) RERPs (yellow regions) screened by ImageJ software.

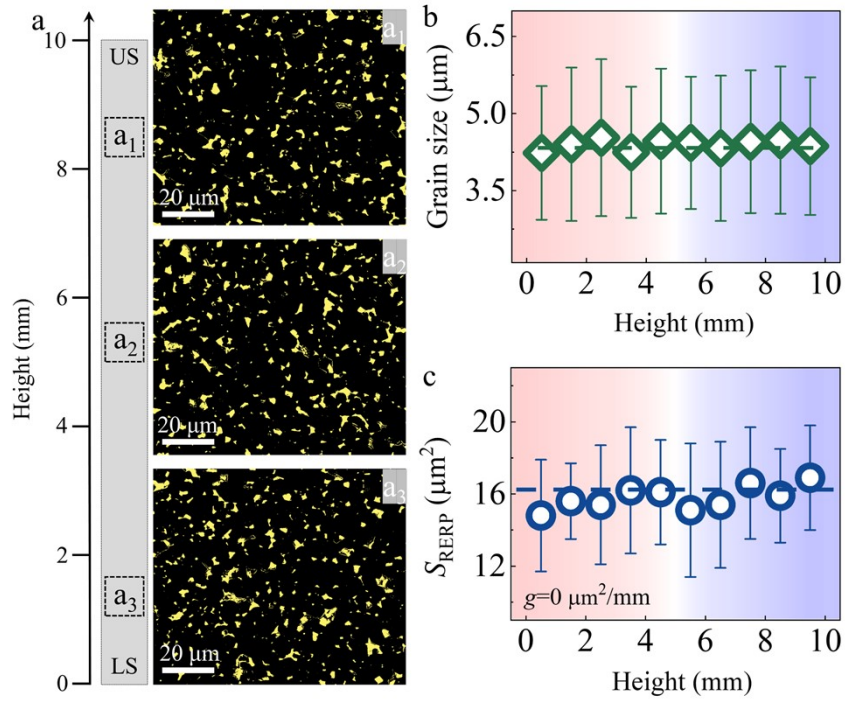


**Fig. S3** Structural characterization of RERPs within G-0.  $a_1$ - $a_3$ ) Screened RERPs images from US (stress-free) to LS (stress-free). Variation of average grain sizes (b) and average area of large-sized RERPs (c) along the height from the LS to the US region at the annealed state.

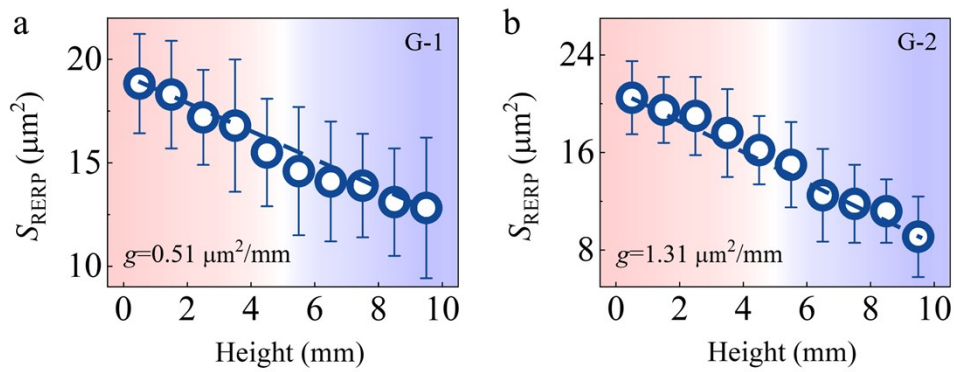


**Fig. S4** Variation of average area of large-sized RERPs for G-1 (a) and G-2 (b) along the height from the LS to the US region at the annealed state.

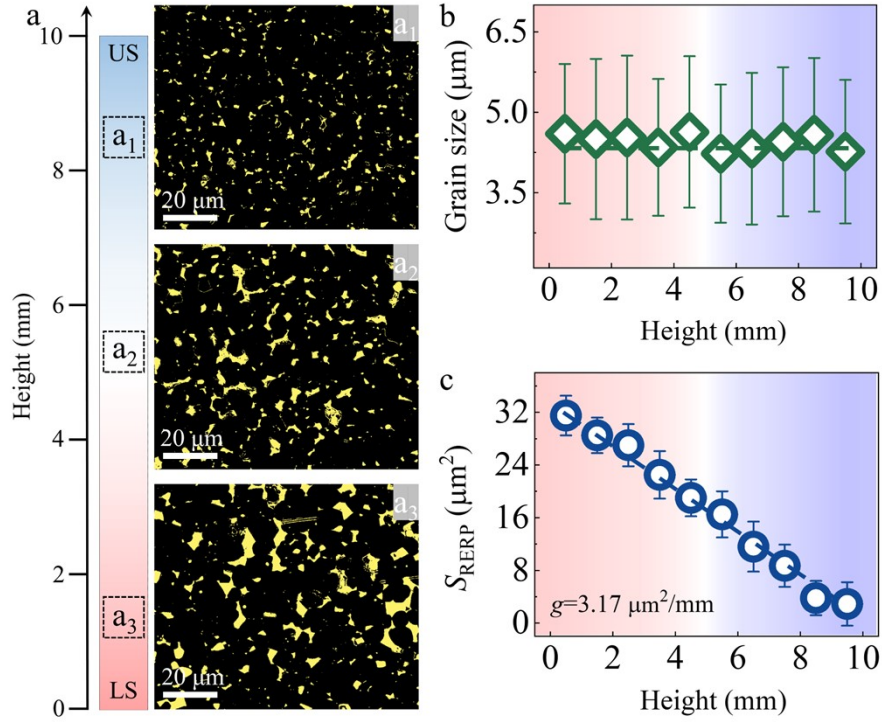


**Fig. S5** Structural characterization of RERPs within G-4 ( $l=35$  mm).  $a_1$ - $a_3$ ) Screened RERPs images from US (compressive stress) to LS (tensile stress). Variation of average grain sizes (b) and average area of large-sized RERPs (c) along the height from LS (tensile stress) to US (compressive stress) at the annealed state.

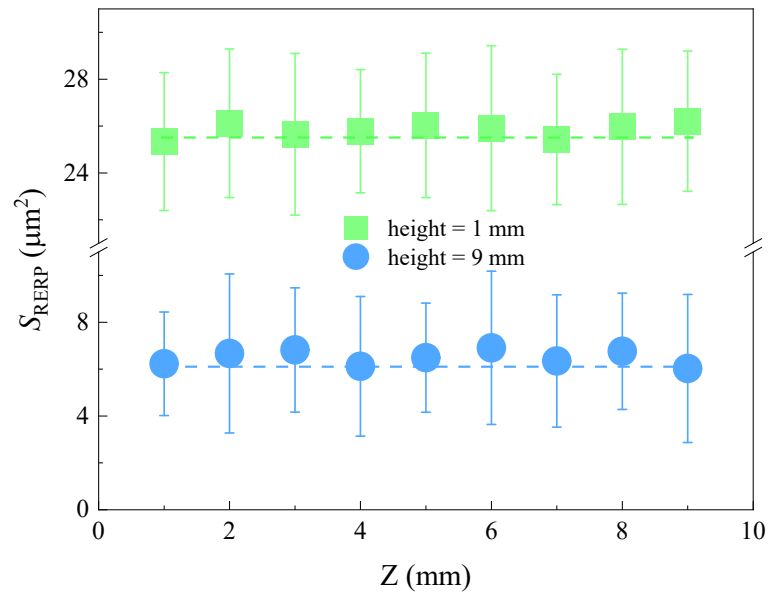


**Fig. S6** RERP size distribution of G-3 XZ plane along the z-axis, where green squares represent a

height of 1 mm, and blue circles represent a height of 9 mm.

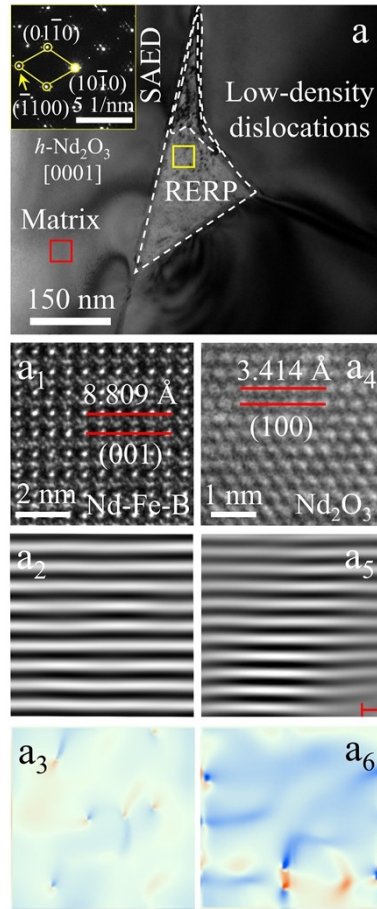


**Fig. S7** Bright-field TEM images of G-0 at the as-sintered state. The inset shows selected area electron diffraction (SAED) pattern performed on the yellow (RERP) rectangle.  $a_1$ - $a_6$ ) HRTEM images of the matrix phase ( $a_1$ ) and RERP ( $a_4$ ), corresponding inverse Fourier transform (IFT) images ( $a_2$ ,  $a_5$ ) and strain maps ( $a_3$ ,  $a_6$ ).

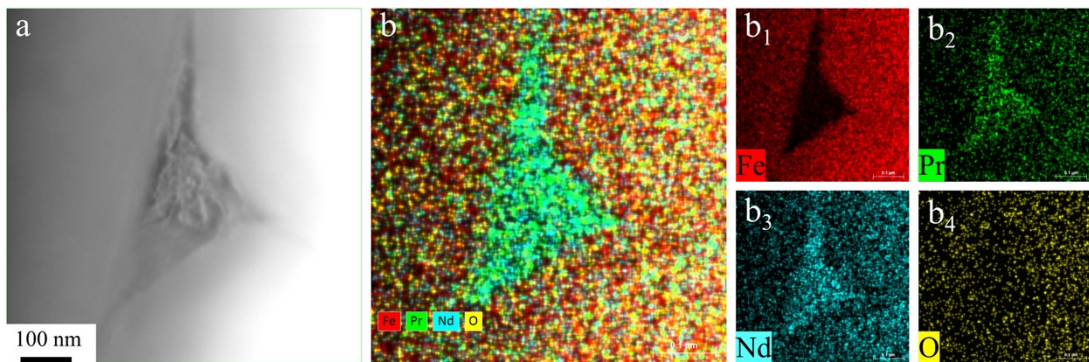


**Fig. S8** Scanning transmission electron microscopy (STEM) image (a), elemental distribution maps

of mixed Pr, Nd, Fe, O (b), Fe (b<sub>1</sub>), Pr (b<sub>2</sub>), Nd (b<sub>3</sub>), O (b<sub>4</sub>).

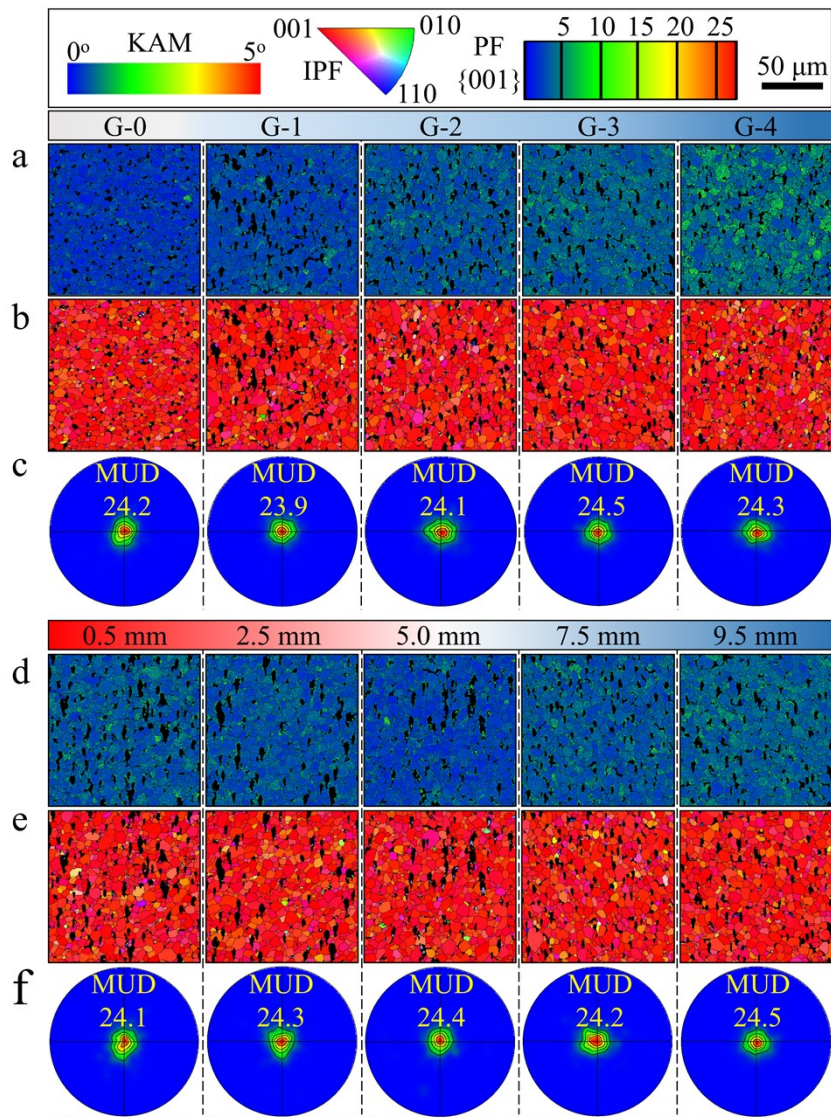


**Fig. S9** KAM maps (a), EBSD orientation maps (b) and Pole figures (c) of as-sintered G-0 (stress-free), G-1 ( $l=26$  mm), G-2 ( $l=29$  mm), G-3 ( $l=32$  mm) and G-4 ( $l=35$  mm) at  $h=9.5$  mm. KAM maps (d), EBSD orientation maps (e) and Pole figures (f) of as-sintered G-3 at  $h=0.5$  mm, 2.5 mm, 5.0 mm, 7.5 mm and 9.5 mm, respectively.

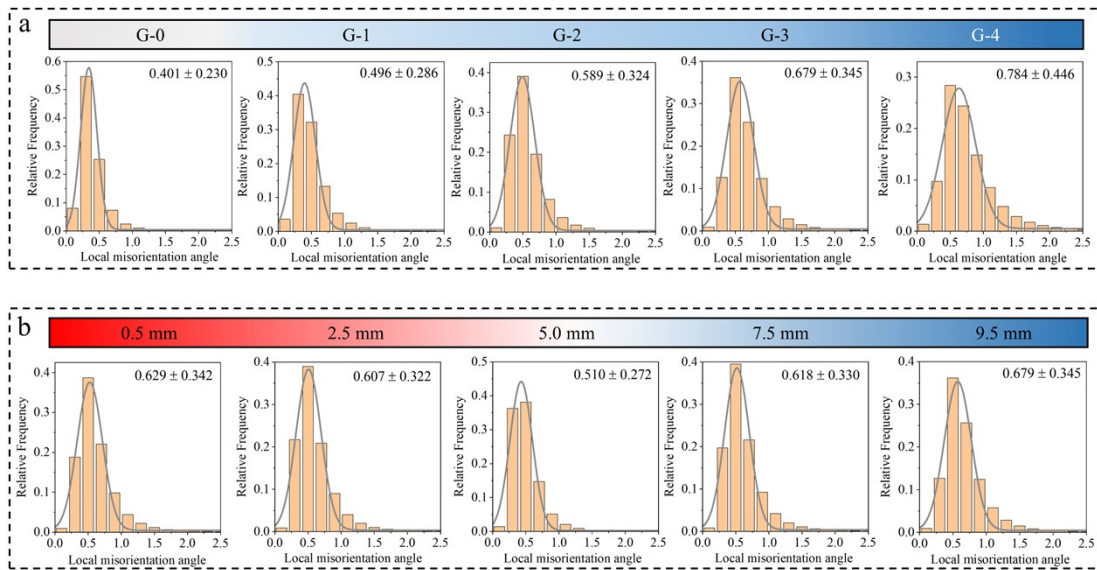


**Fig. S10** a) Local misorientation angle plots of as-sintered G-0 (stress-free), G-1 ( $l=26$  mm), G-2 ( $l=29$  mm), G-3 ( $l=32$  mm) and G-4 ( $l=35$  mm) at  $h=9.5$  mm. b) Local misorientation angle plots of as-sintered G-3 at  $h=0.5$  mm, 2.5 mm, 5.0 mm, 7.5 mm and 9.5 mm, respectively.

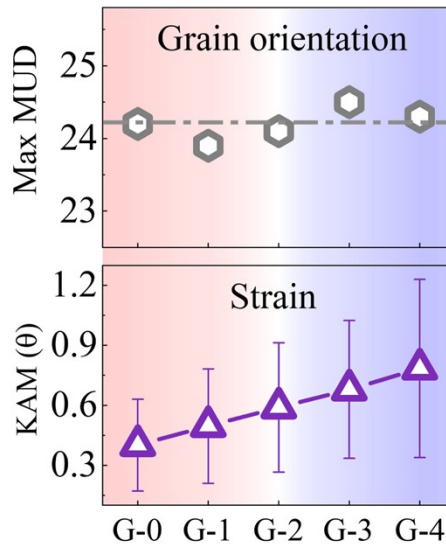


**Fig. S11** Variation of maximum multiples of uniform density (MUD) and kernel average misorientation (KAM) of as-sintered G-0 (stress-free), G-1 ( $l=26$  mm), G-2 ( $l=29$  mm), G-3 ( $l=32$  mm) and G-4 ( $l=35$  mm) at  $h=9.5$  mm.

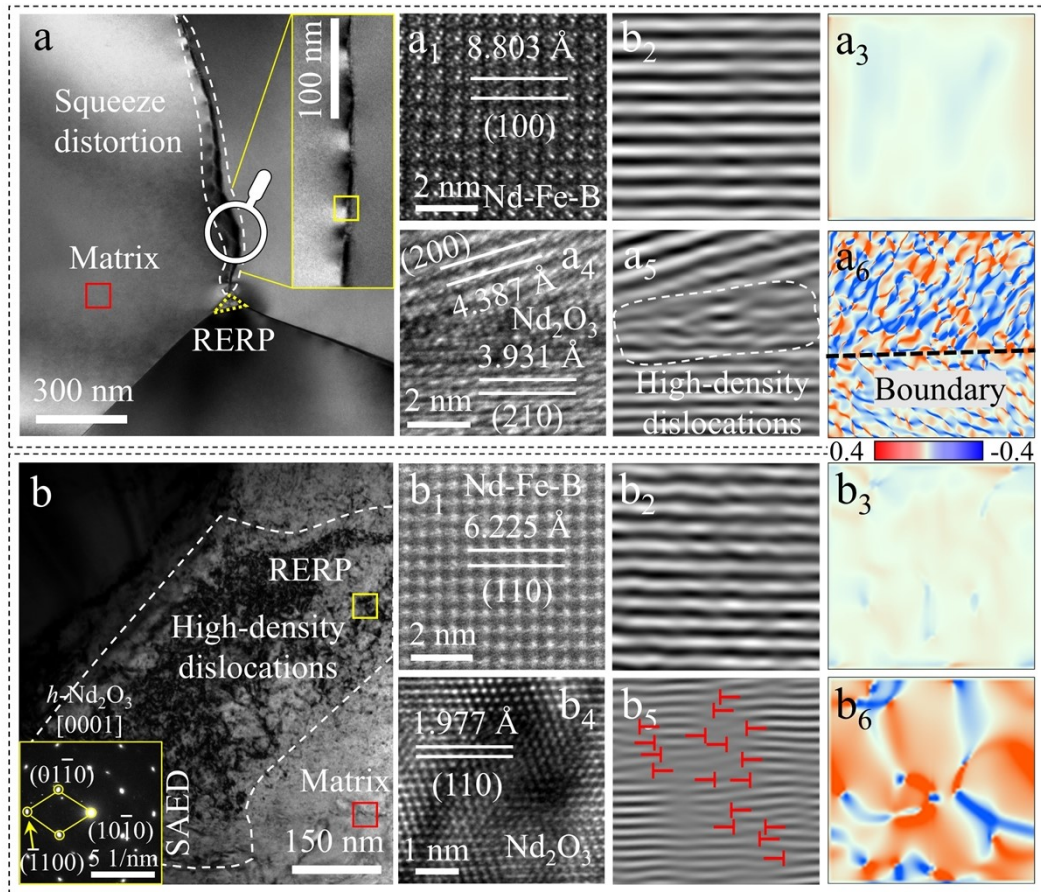


**Fig. S12** Structural characterization of RERPs within G-4 ( $l=35$  mm). a-b) Bright-field TEM images of the US (a) and LS (b) at the as-sintered state. The insets in (a) and (b) show a magnified view of grain boundary and selected area electron diffraction (SAED) pattern performed on the yellow (RERP) rectangle, respectively.  $a_1$ - $a_6$ ,  $b_1$ - $b_6$ ) HRTEM images of the matrix phase ( $a_1$ ,  $b_1$ ) and RERP ( $a_4$ ,  $b_4$ ), corresponding inverse Fourier transform (IFT) images ( $a_2$ ,  $b_2$ ,  $a_5$ ,  $b_5$ ) and strain maps ( $a_3$ ,  $b_3$ ,  $a_6$ ,  $b_6$ ).

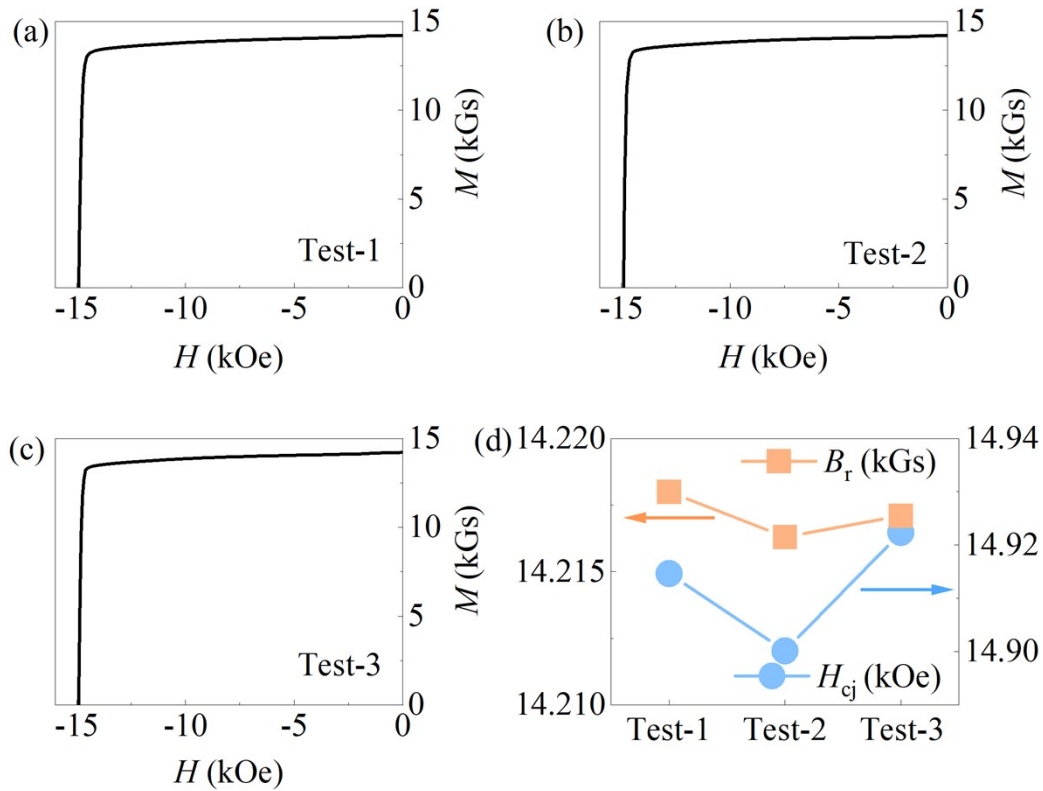


**Fig. S13** Magnetic property characterization of G-3 samples. Demagnetization curves for freshly prepared magnet (a, Test-1, December 2023), natural aging-treated magnet (b, Test-2, 2023.12-2025.03) and magnet treated isothermally at 200 °C for 2 hours (c, Test-3). (d) Comparison of  $B_r$  and  $H_{cj}$  for Test-1, Test-2, and Test-3.

To validate the stability of the gradient RERP, three sets of comparative magnetic performance tests are designed for the G-3 samples: **Test-1 (Control Group)**: immediate testing of the initial magnetic properties of the freshly prepared magnet (December 2023) serves as the baseline reference. **Test-2 (Aging Verification)**: samples from the same batch is tested in the laboratory environment (25 °C, 60% RH) (2023.12-2025.03, equivalent to 15 months of natural ageing treatment) to evaluate the impact of long-term storage on magnetic performance. **Test-3 (Thermal Stability Verification)**: The same batch of samples undergoes isothermal treatment at 200 °C for 2 hours in a vacuum sintering furnace to simulate thermal stability under high-temperature operating conditions. The three test results exhibit no significant differences, demonstrating strong structural stability of the gradient RERP under conventional conditions.

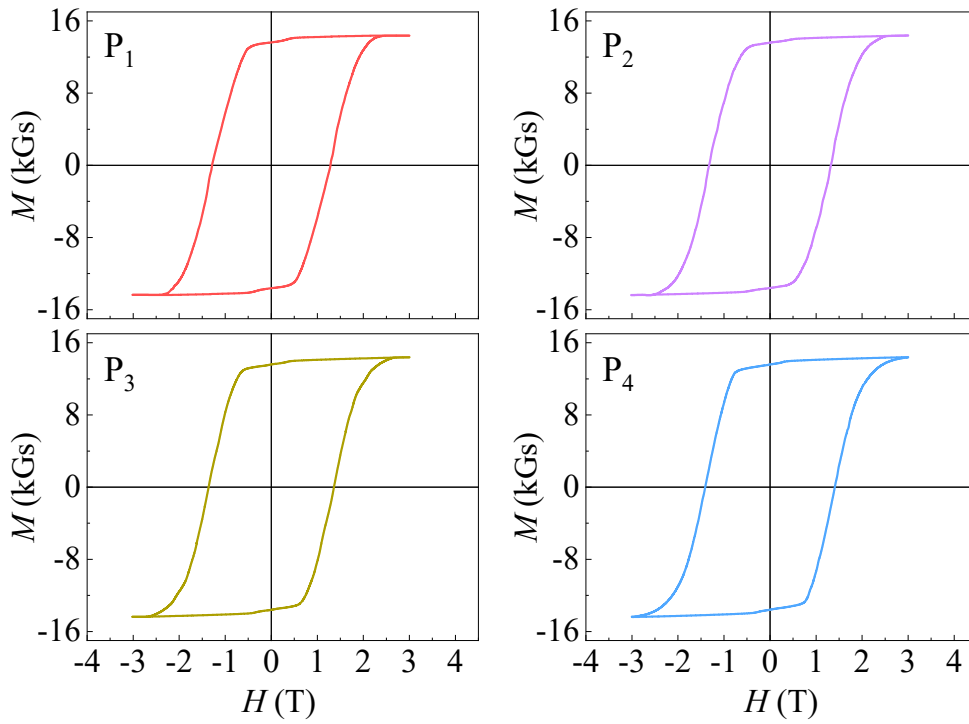


**Fig. S14** Hysteresis loops of P<sub>1</sub>, P<sub>2</sub>, P<sub>3</sub> and P<sub>4</sub> for G-3.

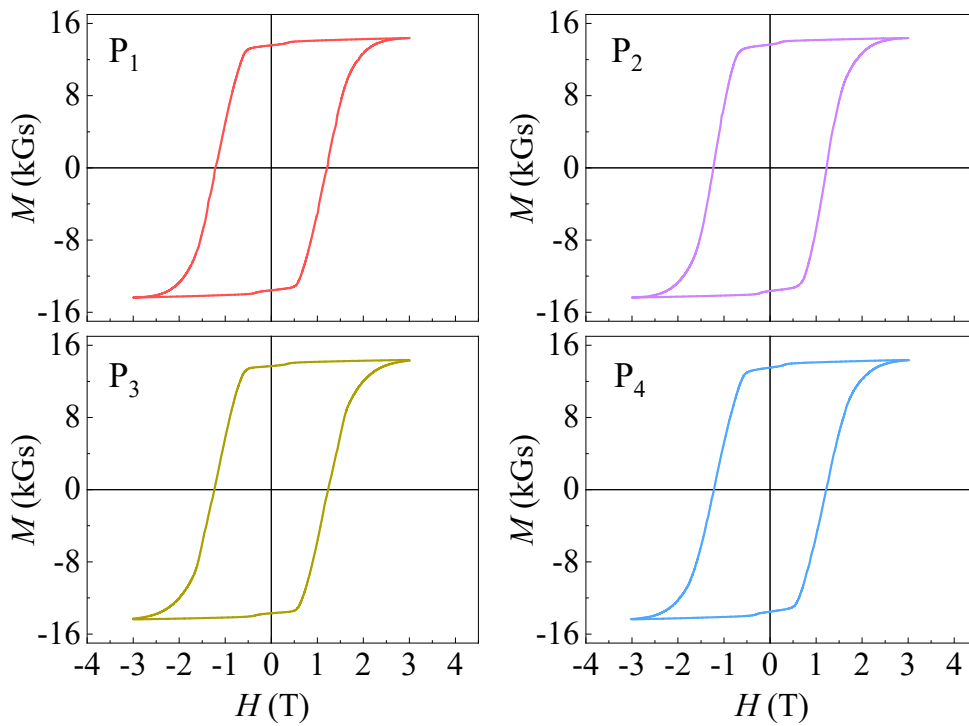


**Fig. S15** Hysteresis loops of P<sub>1</sub>, P<sub>2</sub>, P<sub>3</sub> and P<sub>4</sub> for G-0.

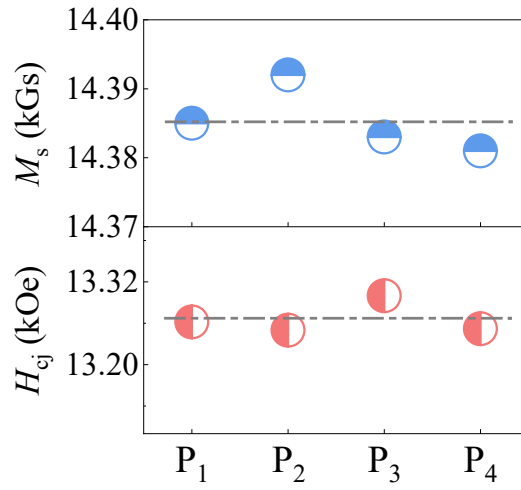


**Fig. S16** Hight-dependent  $M_s$ ,  $H_{cj}$  of G-0.

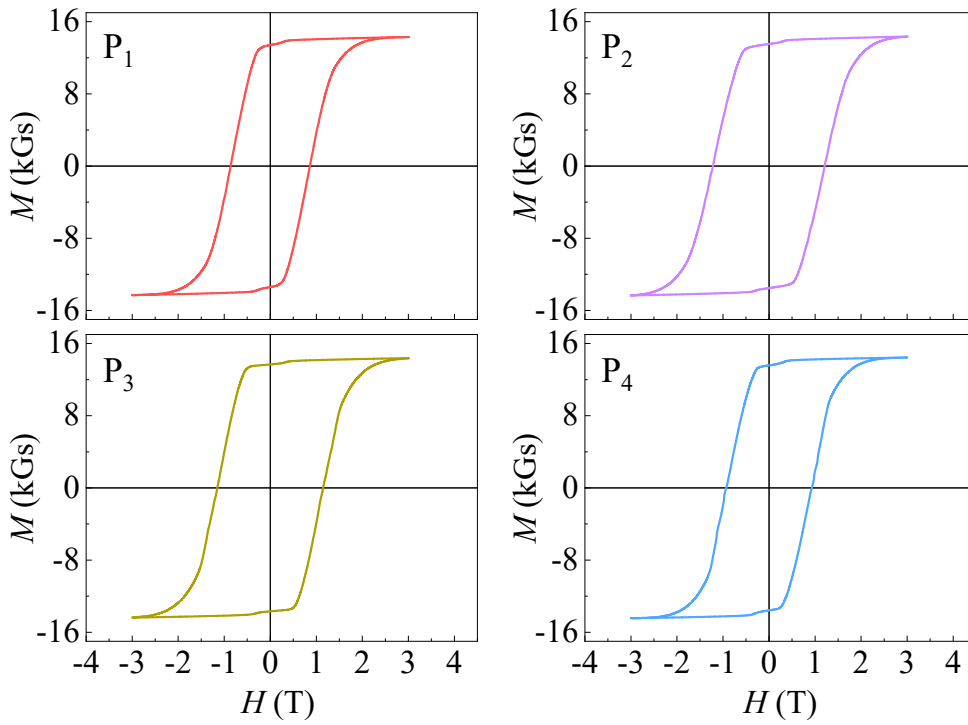


**Fig. S17** Hysteresis loops of  $P_1$ ,  $P_2$ ,  $P_3$  and  $P_4$  for G-4.

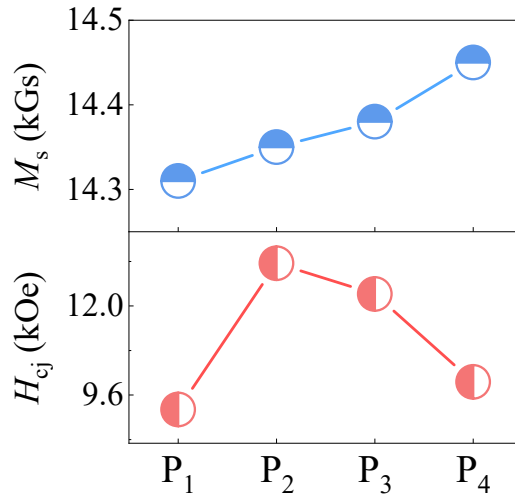


**Fig. S18** Hight-dependent  $M_s$ ,  $H_{cj}$  of G-4.

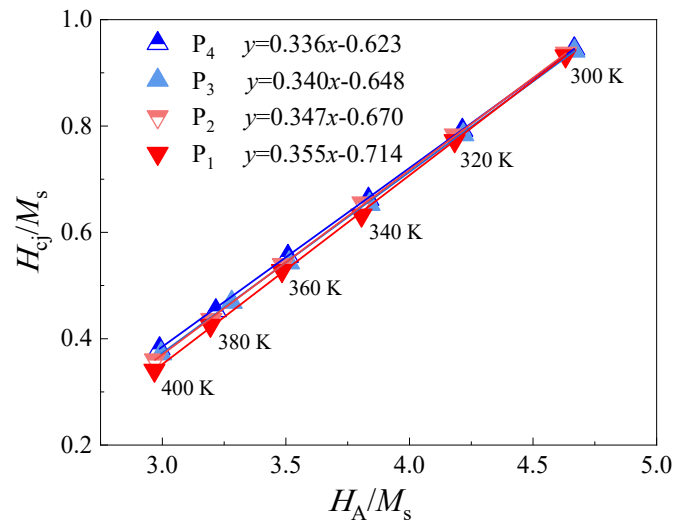


**Fig. S19** The relationship between  $H_{cj}/M_s$  and  $H_A/M_s$  for P<sub>1</sub> to P<sub>4</sub> of G-3 at temperatures from 300 K to 400 K.

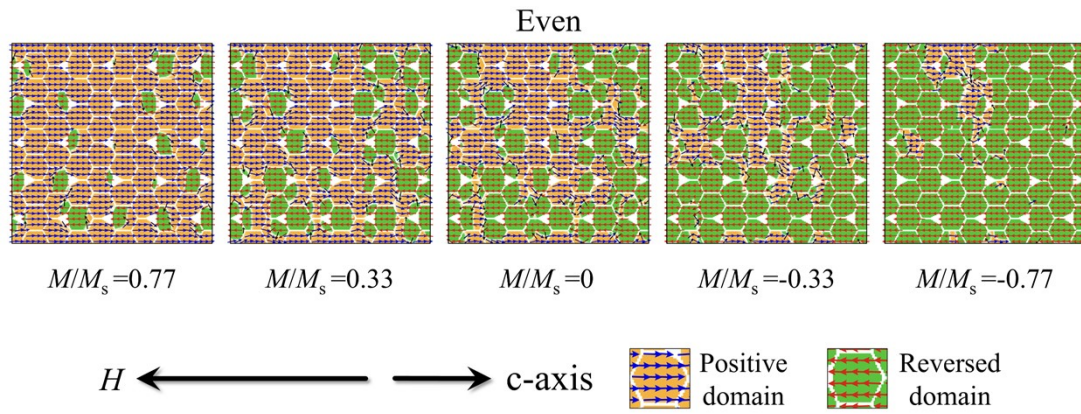


**Fig. S20** Micromagnetic simulations on magnetization reversal of Nd-Fe-B with E-RERPs.

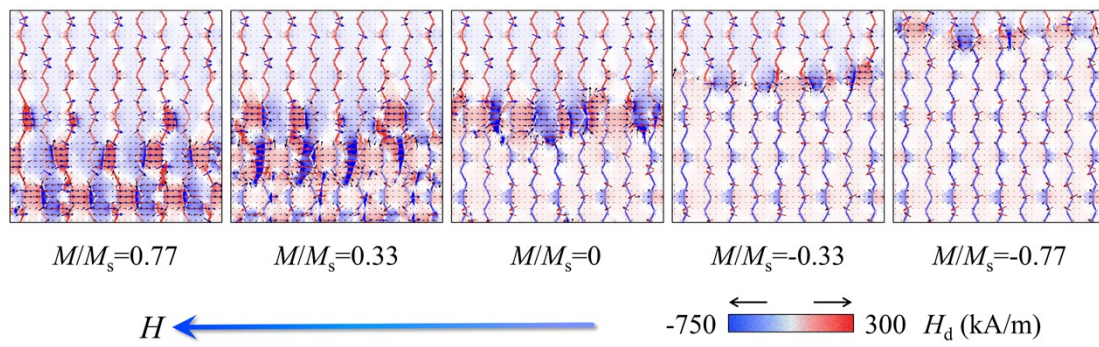


**Fig. S21** Simulations on demagnetizing field of G-RERPs during magnetization reversal.